Infrared Physics & Technology 137 (2024) 105105

Contents lists available at ScienceDirect

Infrared Physics and Technology

journal homepage: www.elsevier.com/locate/infrared

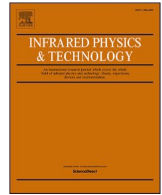

High performance few-layered *h*-BN-based MIS blocks by Fowler-Nordheim tunneling for infrared photodetection

Jiayi Qin [a,1], Ruiqi Jiang [b,c,1], Man Luo [a,b,*], Tiantian Cheng [a], Yuxin Meng [a], Yuanze Zu [a], Jinzhong Zhang [c,*], Johnny C. Ho [d,*], Chenhui Yu [a,*], Junhao Chu [b,c]

[a] Jiangsu Key Laboratory of ASIC Design, School of Information Science and Technology, Nantong University, Nantong 226019, China
[b] Shanghai Institute of Technical Physics, Chinese Academy of Sciences, Shanghai 200083, China
[c] School of Physics and Electronic Science, East China Normal University, Shanghai 200241, China
[d] Department of Materials Science and Engineering, City University of Hong Kong, Kowloon 999077, Hong Kong, China

A R T I C L E I N F O

Keywords:
Few-layered *h*-BN
Fowler-Nordheim tunneling
GaN-based MIS
TCAD simulation
Electrical characteristics

A B S T R A C T

Hexagonal Boron Nitride (*h*-BN) is a promising material for a wide range of applications. Since its discovery, it has been used in nanoelectronic and optoelectronic devices as an optimal substrate for various two-dimensional materials. In addition, *h*-BN is a natural hyperbolic material in the mid-infrared region, where there are few options for photonic materials. To understand the relationships between structure and properties, it is essential to assess the number of layers in *h*-BN at the nanoscale. Here, using a combination of simulation and experiment, we systematically studied on the Fowler-Nordheim tunneling effect in few-layer *h*-BN, and basic physical parameters such as the layer-dependent effective mass are accurately obtained and verified. This work proceeds with a systematic investigation on the design of GaN-based metal/insulator/semiconductor (MIS) blocks with few-layered *h*-BN as insulating layers. It is found that the structural and material properties such as the number of *h*-BN layers, the GaN doping concentration, and the work function of contact metals exert dominant influence on the electrical characteristics of these MIS blocks, while the ideal heterogeneous interfaces of the 2D *h*-BN films mitigate the suffering by non-ideal factors such as interfacial traps and SRH recombination. By comprehensively balancing the mutual constraints of the key factors, this work achieves GaN-based MIS blocks capable of operating under higher voltages, currents, or power conditions compared to their counterparts. This paper aims to provide the fundamental physics of *h*-BN devices and help develop related *h*-BN-based infrared optoelectronics.

1. Introduction

Wide bandgap two-dimensional materials have many excellent properties including high breakdown voltage, low dielectric constant, low defect density, excellent thermal conductivity, high thermal and chemical stability, etc [1–3]. The flat surface is devoid of any dangling bonds and charged impurities, making it an ideal material for functional and innovative nanoelectronic and infrared optoelectronic devices. On the one hand, wide bandgap materials could be used as the blocked barrier layer. Intriguing van der Waals-based unilateral depletion and unipolar barrier detectors proposed by Hu et al. demonstrate a low dark current and exceptional room-temperature detectivity in the visible and mid-wavelength infrared regions [4,5]. Furthermore, this "localized" unipolar barrier was design with novel groove aperture, which was first realized the ultralow spectral crosstalk for 128 × 128 mid-wavelength/long-wavelength two-color infrared detections [6]. This localized field was further verified by the novel broadband photocurrent mapping spectrometer with the focused illuminations from ultraviolet to infrared with the high resolutions up to 0.6 μm, and the minority carrier-sensitive nanoprobe-enhanced mapping system with the illuminated minority carrier spatial resolution up to 30 nm and the dark electrical spatial resolution of 2–10 nm, respectively [5]. On the other hand, wide bandgap materials act as the dielectric or tunneling layers in which Fowler-Nordheim (F-N) tunneling is dominated at high electric fields [7–10]. For instance, Boron Nitride (*h*-BN) has a crystal structure similar to graphene. Gao et al. investigated the vertical structure of graphene/*h*-

* Corresponding authors at: Jiangsu Key Laboratory of ASIC Design, School of Information Science and Technology, Nantong University, Nantong 226019, China (M. Luo).
E-mail addresses: luoman@ntu.edu.cn (M. Luo), jzzhang@ee.ecnu.edu.cn (J. Zhang), johnnyho@cityu.edu.hk (J.C. Ho), ychyu@ntu.edu.cn (C. Yu).
[1] Authors contributed equally to this work.

https://doi.org/10.1016/j.infrared.2023.105105
Received 15 December 2023; Received in revised form 20 December 2023; Accepted 23 December 2023
Available online 9 January 2024
1350-4495/© 2024 Elsevier B.V. All rights reserved.

BN/2D layered semiconductors (2DLSs) and fabricated high-performance photodetectors by utilizing the F-N tunneling effect, whose photoresponses can be tuned from visible to mid-infrared wavelengths, along with advantages such as high detection rate and response rate [11].

With the rapid development of three-dimensional (3D) III-nitrides grown on *h*-BN substrates by van der Waals epitaxy, new avenues are being opened for the advancement and application of novel nitrides devices in optoelectronics and electronics [12–14]. Moreover, the mixed-dimensional integration of 3D and 2D materials provides innovative electronic and optical attributes [15–17]. Lu et al. fabricated graphene/*h*-BN/GaN heterostructure detectors with extremely high responsivity and detectivity where the *h*-BN layer increases the barrier height at the graphene/GaN heterojunction and thus reduces the dark current and enhances the on/off current ratio of the devices [18]. David Arto Laleyan et al. exploited the p-type characteristics of boron vacancies in *h*-BN and firstly demonstrated the Mg-free Al(Ga)N/*h*-BN nanowire LEDs featuring high output power and electrical efficiency [19]. Matthew Whiteside et al. incorporated *h*-BN as gate insulator in MIS-HEMTs to significantly reduce gate leakage current compared to traditional Schottky gate electrodes. The high-quality heterojunction interfaces adjacent to *h*-BN also effectively improve device performance [20]. Obviously, the MIS architecture serves widely as crucial basic blocks in the research of both advanced optoelectronic and power devices. As an insulating layer of MIS block, *h*-BN affects significantly the electrical characteristics of the devices due to the F-N tunneling effect in itself. Considering the development trends in *h*-BN/III-nitride-based devices and the fact that GaN is a representative wide-band semiconductor with high thermal conductivity and stability required in emerging semiconductor research, it is of great importance to investigate the design of high-performance metal/*h*-BN/GaN blocks leveraging the F-N tunneling effect [21,22]. However, there is currently insufficient in-depth understanding on the layer-dependent physical properties of *h*-BN and their impact on device performance. These characteristics can noticeably alter both the threshold voltage (V_{th}) and the on-state current (I_{on}) of devices, and therefore must be comprehensively considered if high-performance GaN-based MIS blocks are desired [23].

In this work, several crucial basic physical parameters associated with the number of *h*-BN layers are calibrated through a combination of simulation and experiment, such as the effective mass. The accuracy of these extracted parameters is further verified by comparing the simulation process parameters with corresponding experimental reports. On this basis, systematical investigations on the design and electrical characteristics of GaN-based MIS blocks employing few-layered *h*-BN as insulating layers are performed. It is found that the current–voltage (*I-V*) characteristics of the MIS blocks are mainly affected by the number of *h*-BN layers (thicknesses), the GaN doping concentration, and the work function of contact metals, while the impact of non-ideal factors such as defects at the heterojunction interfaces or the SRH recombination is dramatically reduced due to the excellent interfacial properties of the 2D layered *h*-BN. The designed GaN-based MIS blocks achieve a maximum V_{th} of 4.28 V, a maximum I_{on} of 2.12 × 10^{-2} A, and a maximum equivalent operating power of 25.8 mW, placing them in a favorable competitive position among similar MIS architectures. This work is meaningful in promoting the application of 2D layered *h*-BN as dielectric and tunneling layers for novel devices in the fields including infrared physics and technology.

2. Simulation models and methods

The electrical characteristics of the MIS blocks in this work are simulated by solving the Poisson equation, the continuity equation for charge carriers, and the drift–diffusion equation. The simulation is performed utilizing the SDevice module of the Sentaurus TCAD software. In the simulation, all the metal/*h*-BN/n-GaN structures are constructed by a GaN thickness of 1.2 μm and a metal thickness of 8 nm. The width of each layer of the device is fixed to 1.5 μm, while the thickness of the *h*-BN layer varies according to the number of layers, as illustrated in Fig. 2a. Numerous experimental researches have reported that the predominant transport mechanism in few-layered 2D *h*-BN films is F-N tunneling [24]. Based on this theory, our investigation centers on examining the impact of layer-dependent F-N tunneling properties on the electrical characteristics of MIS blocks with thin-layer *h*-BN. The mathematical formula for the F-N tunneling model is as [25]:

$$J_{F-N} = AF_{ins}^{2}\exp\left(-\frac{B}{F_{ins}}\right) \tag{1}$$

where $J_{F\text{-}N}$ is the tunneling current density, F_{ins} is the magnitude of the electric field in an insulator, $A = \frac{q^3 m}{8\pi h\varphi_B m^*}$, and $B = \frac{8\pi\sqrt{2m^*}\varphi_B^{\frac{3}{2}}}{3hq}$. *A* and *B* are the physical parameters of the model, primarily related to the effective mass of *h*-BN and the height of the potential barrier across the interface. Calibration based on experimental data are required for the parameter file used during simulations.

The insertion of the traditional dielectric layer in the MIS blocks could introduce numerous additional energy levels on the GaN surface, causing noteworthy Shockley-Read-Hall (SRH) recombination in GaN films, which may impact device performance. In a considerable number of traditional studies related to MIS blocks, the SRH recombination effect often cannot be ignored. Therefore, in order to verify the impact of *h*-BN insertion, we also try to assess the extent to which the SRH recombination works. The SRH model involves carrier recombination through deep-level defects in the energy bandgap, and the equation for the SRH recombination rate is expressed as [26]:

$$R_{net}^{SRH} = \frac{np - n_i^2}{\tau_p\left(n + n_i\exp\left(\frac{E_{trap}}{kT}\right)\right) + \tau_n\left(p + n_i\exp\left(\frac{-E_{trap}}{kT}\right)\right)} \tag{2}$$

where τ_p and τ_n represent the lifetime parameters for bulk holes and electrons, respectively, E_{trap} is the difference between the intrinsic Fermi level and the defect energy level. In the SRH model, it is conventionally set as 0, representing an ideal defect energy level situated at the middle of the bandgap, maximizing the probability of carrier recombination.

In addition, the high doping of a semiconductor will introduce numerous impurity energy levels. These energy levels are located in the energy gap of the semiconductor, and are closely connected to the bottom of the conduction band or the top of the valence band, causing the gap size of the semiconductor to become smaller. Therefore, the Jain-Roulston model is taken into account for this bandgap narrowing effect. As the scattering of ionic impurities influences carrier migration in doped semiconductors, we also incorporate the Arora Model, a mobility model related to doping. The basic parameters of GaN employed in the simulation are outlined in Table 1, primarily derived from experimental or theoretical reports.

3. Results and discussion

Intrinsic physical properties such as thermal conductivity, dielectric constant, band gap, etc. exhibit significant changes if the thicknesses of *h*-BN vary [28]. As an important variable in the parameters of the F-N tunneling model, the layer-dependent effective mass has important research significance [29]. Through the curve fitting simulation of the electrical characteristics of the metal/*h*-BN/metal structure using the F-N tunneling model, we have firstly extracted the trend of effective mass variation with *h*-BN thickness ($d_{h\text{-BN}}$). The detailed steps of this method have been elaborated in our previous work [30]. Fig. 1 presents the pertinent findings, indicating that the effective mass decreases with the number increase of *h*-BN layers which represents the thickness within the range of 4 to 22 layers. Similar trends are also observed in other 2D layered materials, as illustrated in the inset of Fig. 1 [31]. For thinner layers (e.g., 4 layers), the extracted effective mass exhibits a slight

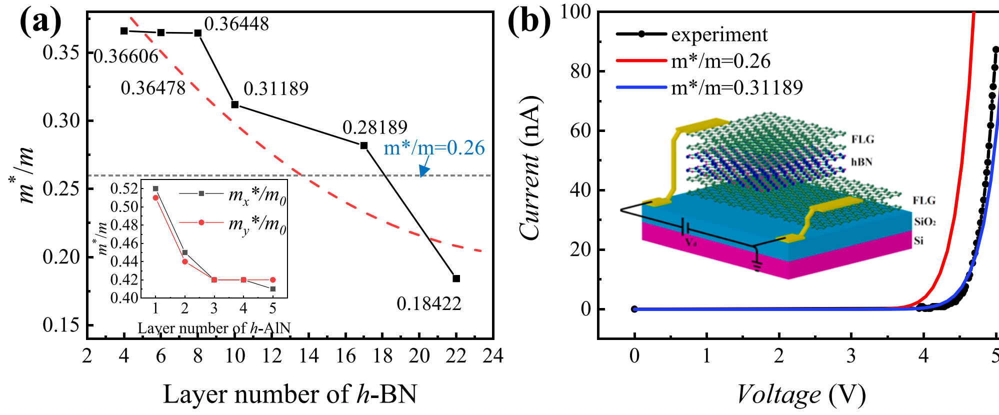

Fig. 1. (a) Variation of effective mass with layer number of h-BN, with an inset shown in [31] illustrating the same trend for 2D h-AlN. (b) I-V curves of simulation and experiment in FLG/h-BN/FLG structure where the number of h-BN layers is 10.

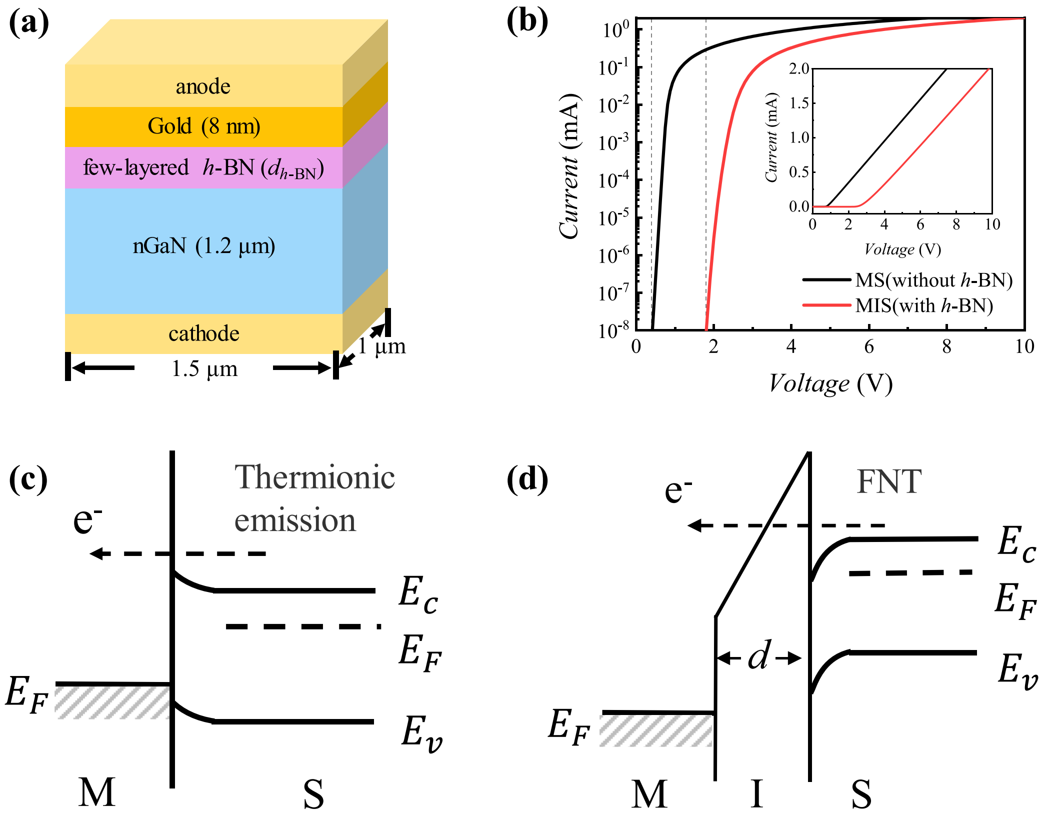

Fig. 2. (a) Schematic structure of the GaN-based MIS blocks with few-layered *h*-BN. (b) Comparison of the *I-V* curves and threshold voltage between the Gold/n-GaN and the Gold/*h*-BN/n-GaN blocks. The energy bands for (c) the Gold/n-GaN blocks and (d) the Gold/*h*-BN/n-GaN blocks under a larger positive bias.

deviation from the trends reported. Part of the reason may be that the measurement error is larger when the layers are thinner in the experiment. Additionally, when the *h*-BN thickness is extremely thin, local regions of the film might undergo direct tunneling instead of complete F-N tunneling, resulting in this discrepancy.

To verify the accuracy of the extracted effective mass, we conduct simulations on the experimentally reported few-layered graphene (FLG)/*h*-BN/FLG structure [32], and have a comparison with its original experimental data. In this structure, the thickness of *h*-BN is 10 layers, equivalent to 3.56 nm, and the corresponding extracted value for the ratio of effective mass to free electron mass (m^*/m) is 0.312. As the reported work function of FLG is about 5.51 eV [33], and the affinity energy of *h*-BN is 2 eV [24], the height of the potential barrier generated by the contact of FLG with *h*-BN is determined to be about 3.51 eV, enabling our simulation to obtain the results as the blue curve shown in Fig. 1b, which are generally consistent with the experimental measurement. In contrast, if the reported effective mass of 0.26 for conventional *h*-BN material is adopted, the simulated red *I-V* curve in Fig. 1b will deviate heavily from the experiment. The comparison shows that the extracted parameters related to the few layers are consistent with experiments and are deemed essential. The relevant parameters such as effective mass and values of F-N model parameters *A* and *B* obtained through the above simulation are listed in Table 2.

Determining the effective mass of few-layered *h*-BN accurately is crucial through a combination of simulation and experiment, attributed to the fact that the size of effective mass encompasses the impact of various factors on the energy bands and its related parameters, such as material dimensions, crystal structures, non-ideal interfacial factors, van

Table 1
Physical models and physical parameters for GaN material used in this simulation [27].

Physical phenomenon	Models	Parameters	Values
BandGap	Temperature dependent bandgap model	Reference Bandgap(E_{g0})	3.53 (eV)
	$E_g(T) = E_g(0) - \frac{\alpha T^2}{T+\beta}$	Reference Electron Affinity(Chi_0)	4.1 (eV)
		Alpha	9.09×10^{-4} (eV/K)
		Beta	830 (K)
Bandgap Narrowing	JainRoulston Model	Coefficient A	1.15×10^{-8} (eVcm)
	$\Delta E_g^0 = A \cdot N_{tot}^{1/3} + B \cdot N_{tot}^{1/4} + C \cdot N_{tot}^{1/2} + D \cdot N_{tot}^{1/2}$	Coefficient B,C,D	0
Mobility	Arora Model	A_{min}(n); A_{min}(p)	115 (cm^2/Vs); 12 (cm^2/Vs)
	$\mu_{dop} = \mu_{min} + \frac{\mu_d}{1+((N_{A,0}+N_{D,0})/N_0)^{A^*}}$with	$\alpha_m(n)$; $\alpha_m(p)$	−1.5 (1); 2 (1)
		A_d(n); $A_d(p)$	1685 (cm^2/Vs); 152 (cm^2/Vs)
	$\mu_{min} = A_{min} \cdot (\frac{T}{300K})^{\alpha_m}$, $\mu_d = A_d \cdot (\frac{T}{300K})^{\alpha_d}$	$\alpha_d(n)$; $\alpha_d(p)$	−1.5 (1); −2.34 (1)
		A_N(n); $A_N(p)$	7×10^{16} (cm^{-3}); 3×10^{17} (cm^{-3})
	$N_0 = A_N \cdot (\frac{T}{300K})^{\alpha_N}$, $A^* = A_a \cdot (\frac{T}{300K})^{\alpha_a}$	$\alpha_n(n)$; $\alpha_n(p)$	3.02 (1); 0.869 (1)
		A_a(n); $A_a(p)$	0.8 (1); 2 (1)
		$\alpha_a(n)$; $\alpha_a(p)$	0.81 (1); −2.311 (1)
Recombination	SRH Recombination	Electron Lifetime (τ_n); Hole Lifetime(τ_p)	0.7×10^{-9} s; 2×10^{-9} s
Other basic Parameters of GaN		Dielectric Constant	8.9
		Electron Affinity	4.1 (eV)
		Effective Electron mass	0.20 (m_0)
		Effective Conduction Band Density of states N_c	2.3×10^{18} (cm^{-3})
		Effective Hole mass	1.25 (m_0)
		Effective Valence Band Density of states N_v	3.5×10^{19}(cm^{-3})

Table 2
Values of F-N model parameters A and B related to few-layered h-BN in GaN MIS block simulation.

$d_{h\text{-BN}}$	layers	m^*/m	A (A/V^2)	B (V/cm)
7.54 nm	22	0.184216	3.980×10^{-6}	8.947×10^7
5.88 nm	17	0.281889	2.601×10^{-6}	1.107×10^8
3.56 nm	10	0.311893	2.351×10^{-6}	1.164×10^8
2.89 nm	8	0.364484	2.011×10^{-6}	1.259×10^8
2.29 nm	6	0.36478	2.010×10^{-6}	1.259×10^8
1.38 nm	4	0.366063	2.003×10^{-6}	1.261×10^8

der Waals forces between layered materials, and in-plane stresses [34]. However, both in experimental and theoretical aspects, obtaining accurate computational and quantitative results influenced by these factors is difficult at present [35].

Firstly, we investigate the changes in electrical characteristics before and after the insertion of h-BN insulating layers between metals and semiconductors, as illustrated in Fig. 2a. The I-V curves of the Gold/n-GaN and the Gold/h-BN/n-GaN MIS blocks are compared in Fig. 2b. The V_{th} (at which the current reaches 1×10^{-11} A) in the MIS blocks is obviously larger than that in Gold/n-GaN blocks, due to a higher barrier introduced by the h-BN insulating layer. The energy bands at higher positive bias in the Gold/n-GaN and the MIS blocks are given in Fig. 2c and 2d, respectively. The electrons for MIS blocks have to tunnel through a triangular barrier of considerable thickness in the h-BN, caused by the downward movement of the energy bands under a positive bias. However, the height of the potential barrier of the Gold/n-GaN, which is already very thin in thickness, still drops in response to the applied positive voltage, allowing easier electron transport and thus lowering the threshold voltage.

The electrical properties of the MIS blocks are then investigated after introducing h-BN with various thicknesses. The I_{on} under a positive bias of 7 V is used as a criterion to facilitate the comparison of the operating current, as reported in literatures [36]. The I-V curves show that V_{th} increases with h-BN thicknesses, while I_{on} changes in the opposite direction as shown in Fig. 3a. This result can be explained by the F-N theory illustrated in Eq. (1), where the components of the equation exhibit an inverse proportionality to the thickness of h-BN. In this work, the on-state resistance (R_{on}) [37] is determined by the slope of the region showing better linearity in the I-V curves when the MIS blocks are turned on, which responds to the I_{on} growth rate. The current changes in the opposite trend of resistance when the voltage is fixed so that R_{on} increases with h-BN thicknesses, as shown in Fig. 3b. The magnitudes of the electric field in h-BN (F_{ins}) under different positive bias caused by the thicknesses of the insulating layer are exhibited in Fig. 3c, which is the multiplication of the potential difference between the two sides of the h-BN and the reciprocal of its thicknesses. In the case of high electric field, the analysis of h-BN breakdown process needs to consider the spatial distribution of charge carriers and fields. Hu and Xie et al. first proposed the finest model of impact ionization currently available based on Fermi golden rule impact ionization model in 2021, which considers the influence of real-time spatial coordinates of charged particles and is one of the most important analytical models for studying the microscopic mechanism of impact [38]. The breakdown strength with different thicknesses of h-BN is extracted, defined as the electric field of h-BN with the device turned on, exhibiting a monotonic increase with the thicknesses of h-BN, which is basically consistent with the trend and value reported in literatures [39–43] as shown in Fig. 3d. The consistency affirms the accuracy of our simulation parameters and reflects the precision of the basic physical parameters employed.

Different GaN doping concentration result in varying carrier concentrations, which inevitably has an impact on the F-N tunneling effect and related properties in h-BN. The lower limit of GaN doping concentration is taken as 10^{14} cm^{-3}, considering that unintentionally doped GaN demonstrates n-type behavior, and the carrier concentration aligns approximately with this value. The upper limit is taken in consideration of the experimentally achievable doping concentration of 10^{18} cm^{-3}. Furthermore, if the doping concentration exceeds 10^{19} cm^{-3}, the GaN transitions into a degenerate semiconductor state, leading to a substantial simulation error. As a result, the electrical properties of the Gold/h-BN/n-GaN blocks are analyzed with the GaN doping concentration ranging from $10^{14} \sim 10^{18}$ cm^{-3}. The V_{th} remains consistently around 2.7 V with slight variation when the thickness of h-BN is 3.56 nm, as shown in Fig. 4a. This phenomenon exists for all the MIS blocks of the above range of GaN doping concentration as the mapping in Fig. 4b, attributing to the fact that the height of contact barrier between GaN and h-BN essentially remains constant and is unaffected by doping concentration as in Fig. 4c. However, the R_{on} of the device significantly reduces with the rising GaN doping concentration as shown in Fig. 4a, since more electrons are involved in the F-N tunneling process under higher GaN doping concentration, resulting in consistent increase current of the devices under the same positive bias. High GaN doping concentration leads to a more distinct slope of the conduction band barrier in h-BN before the devices are turned on explained from the perspective of energy bands in Fig. 4c. The actual thickness of the potential barrier for

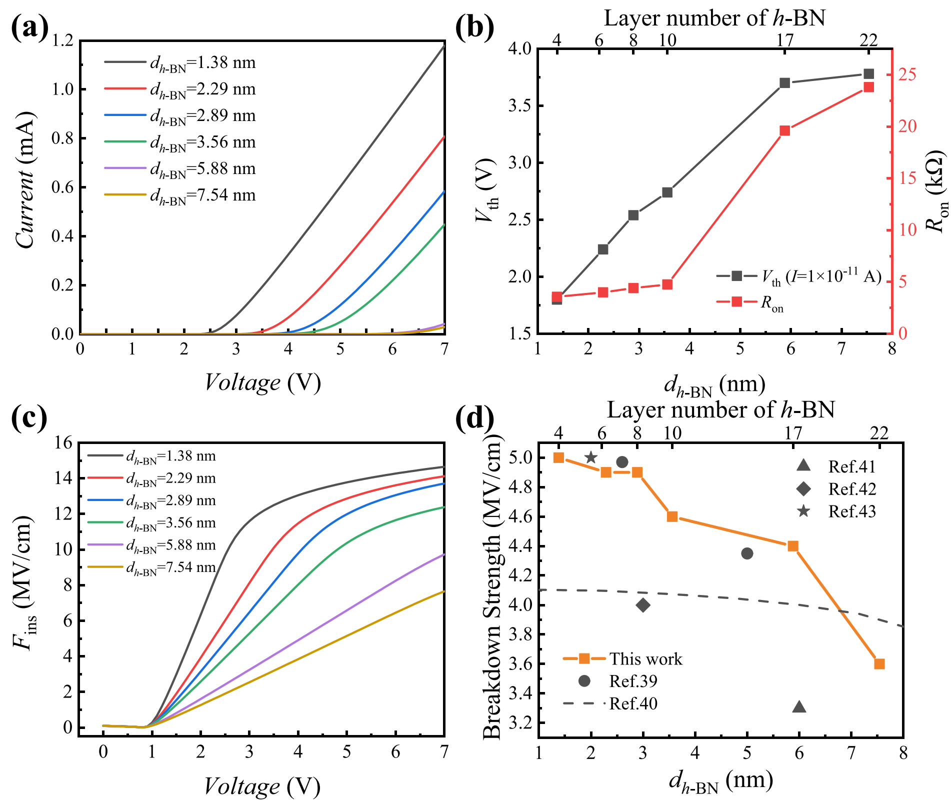

Fig. 3. (a) *I-V* curves of the GaN-based MIS blocks with different thicknesses of *h*-BN. (b) Variations of the threshold voltage and the on-state resistance with different thicknesses of *h*-BN. (c) Variations of electric field with different thicknesses of *h*-BN. (d) Comparison of the breakdown strength of *h*-BN between this work and corresponding experimental reports under the GaN doping concentration of 1×10^{16} cm^{-3}.

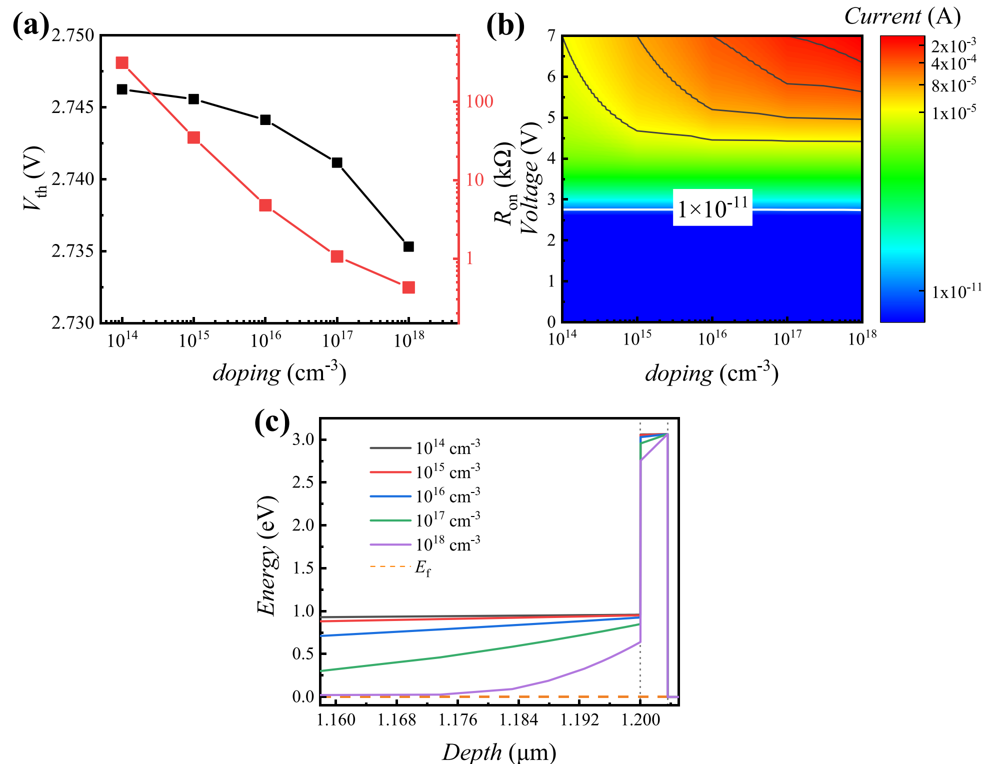

Fig. 4. (a) Threshold voltage and on-state resistance with different GaN doping concentration. (b) The mapping of *I-V* curves for different GaN doping concentration in the GaN-based MIS blocks. (c) Partial conduction band structures with different GaN doping concentration under no positive bias, where depth represents the distance from the point to the cathode along the direction from cathode to anode.

electron tunneling of the Gold/*h*-BN/n-GaN becomes thinner when the devices are applied to positive bias, making the devices more prone to tunneling phenomena and achieve higher current.

In addition, different Schottky barrier heights formed by different metals with different work functions (*WF*) affect the electrical properties of the MIS blocks when they are contacted with *h*-BN, as shown in Fig. 2d. We select platinum ($WF = 5.6$ eV) with a larger work function and tungsten ($WF = 4.6$ eV) with a smaller work function for comparison [44,45]. We simulate the electrical characteristics of the MIS blocks in different cases and observe a consistent trend. Fig. 5a shows the influence of three commonly used electrode metals on the device when the thickness of *h*-BN is 2.89 nm and the GaN doping concentration is 1×10^{18} cm^{-3}. It is found that both V_{th} and R_{on} increase as the metal work function increases, while the I_{on} decreases in the device. From Fig. 5b we can see that a higher barrier lifts across the interface of *h*-BN and GaN occurs when the metal work function becomes larger, leading to a larger applied voltage to initiate the device, and a decreased I_{on} to appear accordingly. In 2022, Wang and Hu et al. demonstrated an excellent uncooled mid-wave infrared blackbody response based on a vertical fully depleted heterosandwiched structure with optical and electrical combined manipulations, solving the problems of low quantum efficiency and large dark current of 2D photodetectors [46]. The vertical device configuration with atomic thin photocarrier transport distance could realize the fast response speed and high photocarrier collection efficiency. The wide effective detection spectral range was realized in visible and mid-infrared range respectively.

Interface defects are one of the most critical factors limiting the performance and stability of conventional devices. Interface defects in experiments are mostly caused by structural damage, oxidation defects or dangling bonds. The *h*-BN has excellent properties of the flat atomic surface, no dangling bonds and charged impurities, and low interfacial defect states when integrated with other materials. As evident from Fig. 6a, the interface between conventional dielectrics and III-nitrides usually has a high density of trap states up to 10^{14} cm^{-2}eV^{-1} [47–54]. In contrast, the defect states at the *h*-BN/GaN interface are relatively small, with values around 4.3×10^{11} cm^{-2}eV^{-1} [55]. In the simulation, we define the defects or traps at the *h*-BN/GaN interface using the Fixed Charge model. Fig. 6b shows the *I-V* curves of the device under two cases ($d_{h\text{-BN}} = 3.56$ nm & $doping = 1 \times 10^{18}$ cm^{-3} and $d_{h\text{-BN}} = 2.89$ nm & $doping = 1 \times 10^{16}$ cm^{-3}) with different trap densities. Hu et al. for the first time proposed the modified analytical model of trap assisted tunneling and band to band tunneling dark currents for the HgCdTe infrared detectors, significantly improving the modeling accurate of temperature-dependent dark current in infrared detectors [56]. In 2011, continuously Hu et al. proposed the updated modeling formula for trap assisted tunneling,

$$I_{tat} = -A\cdot\frac{\pi^2 q^2 N_t m^*{}_e M^2 (V_{bi} - V_d)}{h^3 (E_g - E_t)} exp\left(-\frac{\sqrt{3}\,E_g^2 F(a)}{8\sqrt{2}\,qPE}\right) \tag{3}$$

$$F(a) = \frac{\pi}{2} + \sin^{-1}(1-2a) + 2(1-2a)\sqrt{a(1-a)} \tag{4}$$

$$a = E_t/E_g \tag{5}$$

which has become a generally accepted model of trap assisted tunneling in narrow band gap materials. Based on this analytical model, we find that trap assisted tunneling has a significant impact on *h*-BN MIS system [57]. Compared to the ideal case (*traps* = 0), these curves largely overlap each other, reflecting the clean *h*-BN interface of the 2D layered material producing very small adverse effects when considered in device design.

In MIS structures, the current is typically composed of tunneling current and generation recombination current. Both currents might significantly coexist, or one might predominantly prevail. Fig. 7a shows the energy bands of the SRH recombination process [58], where the electrons and holes do not recombine directly, but rather transit to a third-party energy state for charge neutralization. We explore the role of the SRH model in Gold/*h*-BN/n-GaN structures by comparing the *I-V* curves of devices with the SRH model or not. In Fig. 7b, it is observed that when the thickness of *h*-BN is 2.89 nm, the *I-V* curves overlap entirely and the SRH recombination current can essentially be disregarded, regardless of whether the doping concentration in GaN is 1×10^{16} cm^{-3} or 1×10^{18} cm^{-3}. Because GaN is N-type, applying a positive bias on the metal attracts more electrons toward the *h*-BN/GaN interface, while the hole concentration at this interface is practically zero, leaving no holes to accommodate the electrons. Then SRH recombination current tends toward zero and the value of R_{net}^{SRH} is infinitely close to 0 as well as analyzed in Eq. (2). Fig. 7c compares the magnitude of the SRH recombination rates of Gold/n-GaN Schottky diodes with that of the MIS blocks. We observe that compared to the SRH recombination rate in the pure GaN film, the current recombination effect in the MIS blocks resulting from device turn-on is significantly reduced to essentially zero due to the insertion of the *h*-BN insulating layer. Therefore, the SRH recombination current in this structure can be overlooked in contrast to the current generated by F-N tunneling in the device. Similar findings are also observed in the Au/SiO_2/nSi structure [59].

From these analyses, it is evident that V_{th} exhibits an increasing trend with the increment of *h*-BN thickness or work function of contact metal. Simultaneously, the I_{on} of the device experiences a concomitant decrease. However, achieving a higher V_{th} and a larger I_{on} is imperative to ensure the proper operation of the device in practical applications. To achieve equilibrium between the two physical quantities, we introduce the power figure-of-merit (*FOM*) from literatures. It serves as a comprehensive measure to evaluate the electrical performance of the device and is defined as [60]:

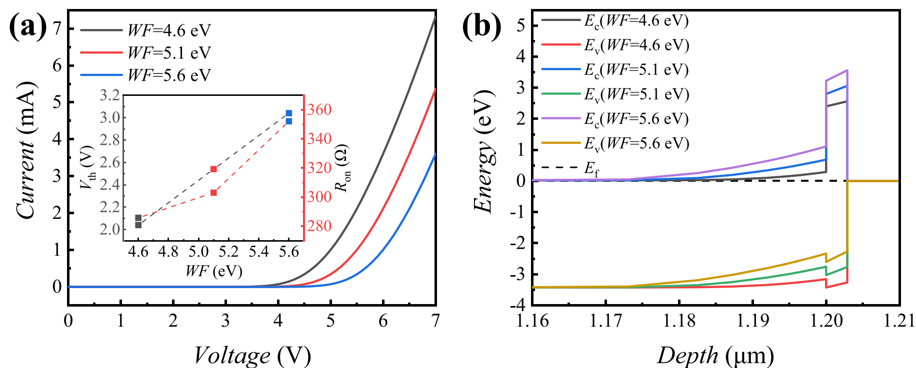

Fig. 5. (a) *I-V* curves with different contact metals in GaN-based MIS blocks, with an inset showing the trend of threshold voltage and on-state resistance. (b) Influence of metal work function on energy band structure without applied bias voltage ($d_{h\text{-BN}} = 2.89$ nm, $doping = 1 \times 10^{18}$ cm^{-3}).

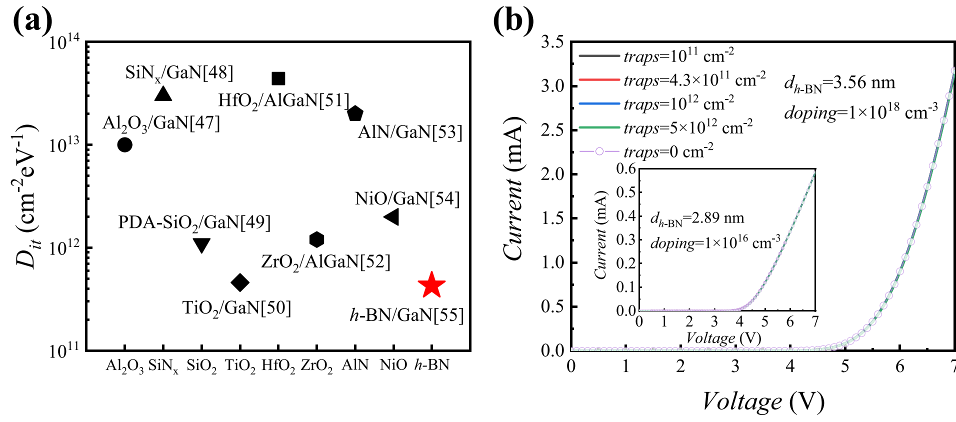

Fig. 6. (a) Comparison of the defect state densities at the *h*-BN/GaN interface and conventional dielectric/III-nitride interfaces. (b) *I-V* curves of GaN-based MIS blocks with different trap densities at *h*-BN/GaN interface ($d_{h\text{-BN}}$ = 3.56 nm, and *doping* = 1 × 10^{18} cm^{-3}). The structural parameters in the inset are $d_{h\text{-BN}}$ = 2.89 nm, and *doping* = 1 × 10^{16} cm^{-3}.

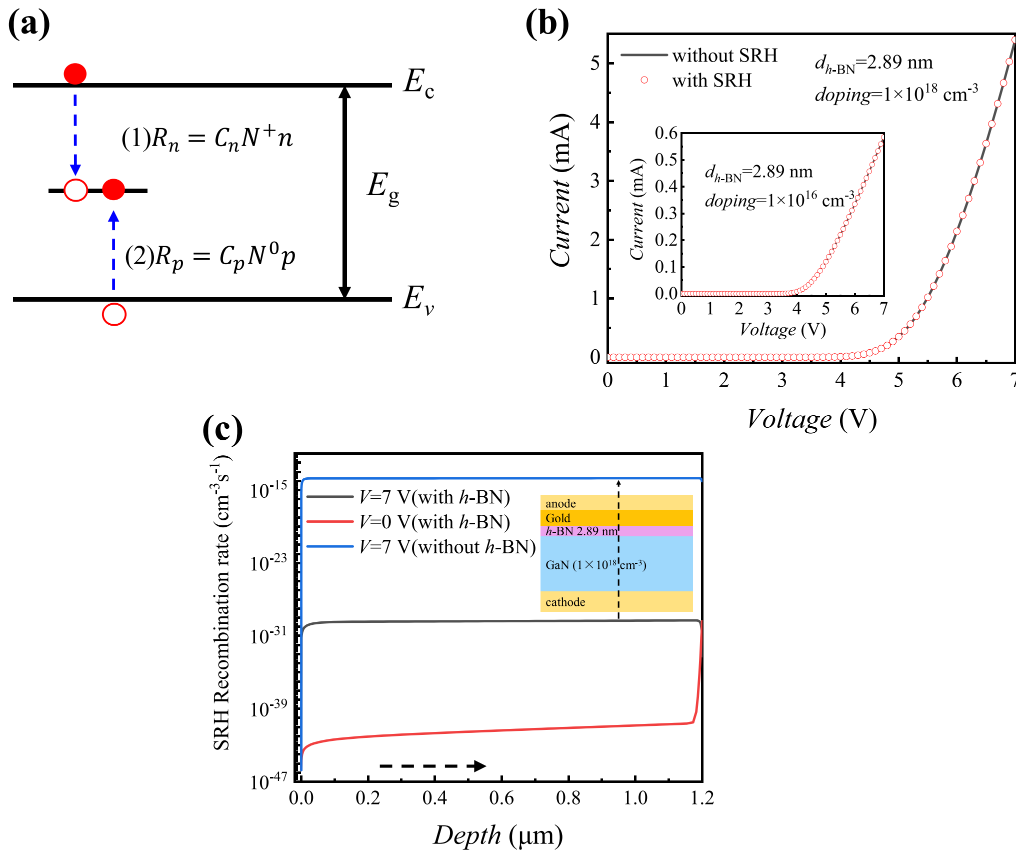

Fig. 7. (a) Schematic of the energy bands of the SRH recombination process. (b) *I-V* curves of GaN-based MIS blocks with and without the SRH model. (c) Comparison of the SRH recombination rates magnitude in the device under a bias voltage of 7 V, which extracted from the location of the dotted line in the insertion.

$$FOM = \frac{V_{th}^2}{R_{on}} \tag{6}$$

We anticipate obtaining a greater V_{th} and I_{on} to achieve a higher *FOM*, signifying the capability of the device to endure elevated electrical power. In Fig. 8, a summary is presented for all *FOM* values obtained under various conditions, including different contact metals, *h*-BN thicknesses, and the GaN doping concentration. These results are presented through line and mapping plots for a thorough comparison. Examining the line graphs, we discern that the *FOM* of the MIS block consistently exhibits a monotonic increase with GaN doping concentration. Besides, the *FOM* values in this structure unfold a pattern of initial increase followed by a subsequent decrease with the increase of *h*-BN thickness, at higher doping concentrations. This behavior is attributed to the fact that V_{th} and R_{on} do not increase at the same rate though both of them tend to increase with the *h*-BN thickness, as illustrated in Fig. 3b. This finding underscores the close correlation between *h*-BN tunneling properties and the number of layers. It indicates that an ideal number of layers or thickness is crucial, as only in this case can electrons maintain a certain number of tunneling particles while upholding a certain size of tunneling probability [10]. Comparing Fig. 8a, b, and c, it becomes evident that the device achieves its maximum *FOM*

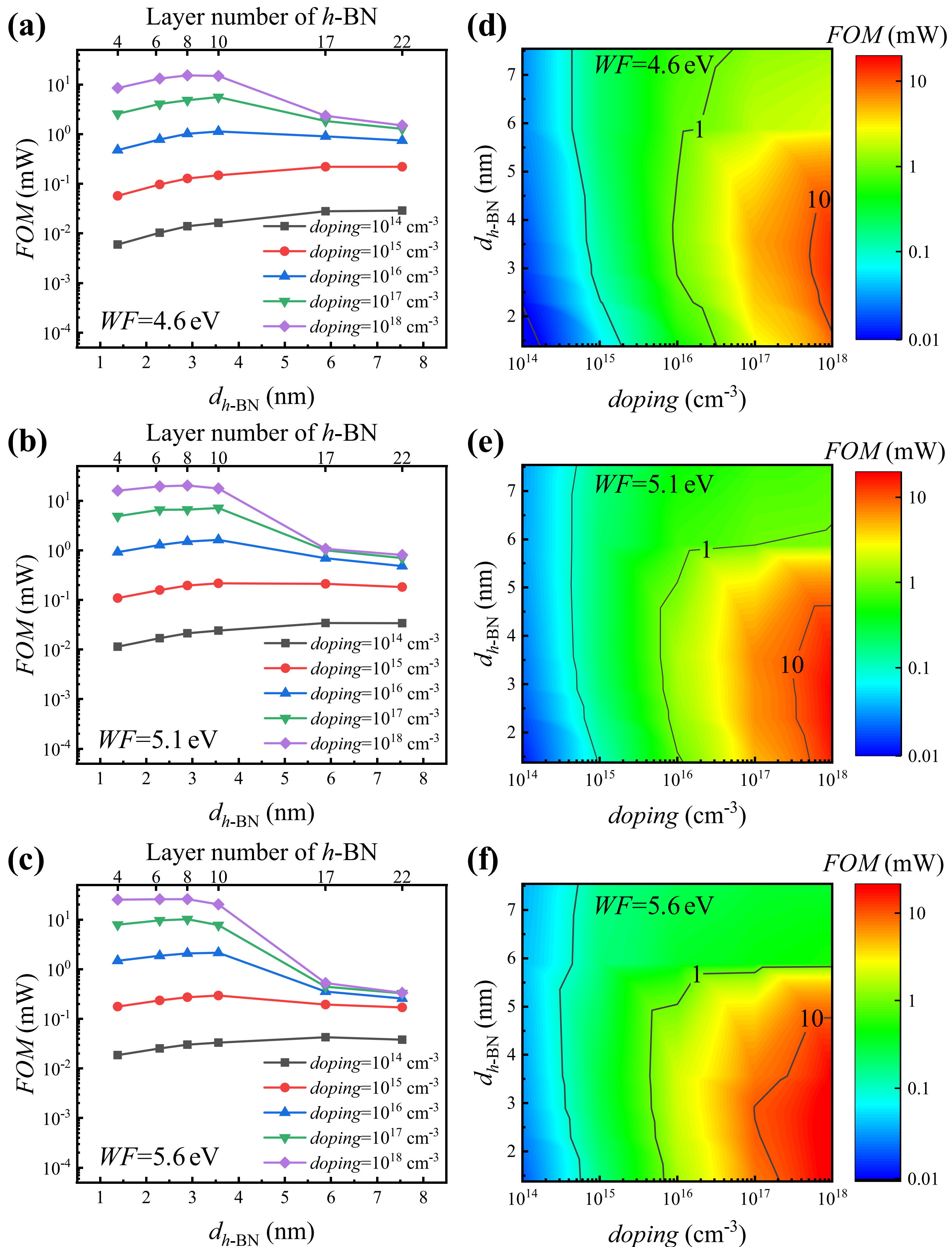

Fig. 8. Line and mapping diagrams of figure-of-merit under different work function, including (a, d) 4.6 eV, (b, e) 5.1 eV, and (c, f) 5.6 eV.

of 25.8 mW when utilizing platinum as the metal contact, with an *h*-BN thickness of 2.89 nm and a GaN doping concentration of 1×10^{18} cm^{-3}. In the three mapping diagrams (Fig. 8d, e, f), it is evident that within the MIS blocks, there is a notable increase in the *FOM* as the *WF* of the metal rises, and a more accessible equilibrium between V_{th} and I_{on}, implying wider range of *h*-BN thickness and GaN doping concentration options.

Fig. 9 quantitatively illustrates the impact of the *WF*, *h*-BN thickness, GaN doping concentration, interface traps densities, and SRH effect on the *FOM*, V_{th}, and I_{on} of the GaN-based MIS blocks through calculations employing the control variable method. As an example of calculating the

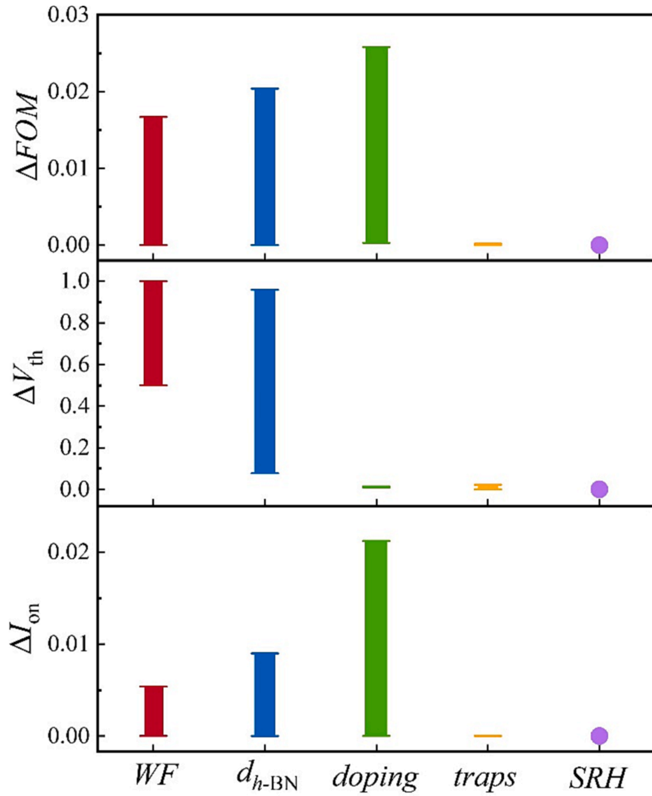

Fig. 9. Scope of the effect of each physical parameter on figure-of-merit, threshold voltage, and on-state current in GaN-based MIS blocks.

impact of *WF* on *FOM* values, we observe the maximum and minimum *FOM* values under various *WF* conditions while parameters such as *h*-BN thickness and GaN doping concentration kept constant. Subsequently, the absolute difference is computed, and a comprehensive comparison of all data is performed to obtain the impact range of *WF* on *FOM* (Δ*FOM*). The figure illustrates that the GaN doping concentration exhibits the most significant impact on the *FOM*, while exerting essentially no influence on the V_{th}. Meanwhile, the selection of metal and the thickness of *h*-BN in the MIS significantly affect each performance of the devices. Differently, the concentration of traps at the *h*-BN/GaN interface, as well as the SRH effect, essentially have no discernible effect on the electrical characteristics of MIS blocks due to the excellent surface properties of 2D *h*-BN.

In this research, we discern that judicious exploitation of the layer-dependent properties of *h*-BN enables the design of MIS blocks catering to diverse performance requirements. The achieved maximum V_{th} of 4.28 V stands at a relatively high level compared to the results reported. Furthermore, the maximum I_{on} for this block reaches up to 2.12×10^{-2} A, which is one of the excellent figure-of-merit. Considering the perspective of overall power handling capacity, the *FOM* of the block attains a peak value of 25.8 mW, surpassing those reported in recent literature for MIS blocks involving GaN or other traditional dielectric layers [9,61–68], as vividly illustrated in Fig. 10. The specific parameters of the structures corresponding to the optimal electrical properties are presented in Table 3. For GaN-based MIS blocks, the structure can be systematically designed to accommodate diverse scenarios, by taking into account factors such as the few-layered *h*-BN thickness, the GaN doping concentration, and the *WF* of contact metals.

Compared with conventional insulating layers, *h*-BN has excellent properties such as easily controllable thickness and atomically flat surface. When employed as a dielectric layer, MIS blocks can be designed for various functions, encompassing ultra-thin rectifiers, memories, and photodetectors. Theoretically, when used as an infrared detector, the

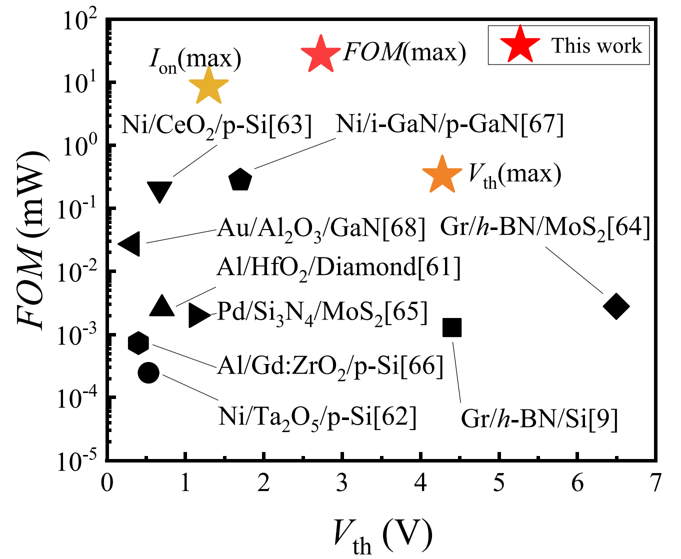

Fig. 10. Comparison of figure-of-merit values of this work with reported values for similar MIS blocks.

Table 3
The GaN-based MIS block parameters corresponding to optimal performance for each electric property.

performance (max)	values	$d_{h\text{-BN}}$ (nm)	layers	*doping* (cm^{-3})	*WF* (eV)
I_{on}	2.12×10^{-2} A	1.38	4	1×10^{18}	4.6
V_{th}	4.28 V	7.54	22	1×10^{14}	5.6
FOM	25.8 mW	2.89	8	1×10^{18}	5.6

metal/*h*-BN/GaN block will experience pronounced suppression of carrier transport due to the substantial electron barrier at the *h*-BN/GaN interface, facilitated by the introduction of *h*-BN. This results in the attainment of extremely low dark current, and improved detector performance in terms of detectivity and responsivity. At the same time, higher on/off ratios in light detection can be achieved with the *h*-BN based structure. Consequently, this configuration ensures exemplary low-power light detection at room temperature.

4. Conclusions

This work initiates the calibration and extraction of basic parameters such as the effective mass in the simulation model through a comparative analysis with relevant experimental data. Building upon this foundation, the design of the MIS block based on GaN with few-layered *h*-BN as the insulating layer is systematically investigated. The findings indicate that the number of layers of *h*-BN, the GaN doping concentration, and the *WF* of the contact metal have the dominant influence on the *I-V* characteristics of the MIS blocks. Additionally, owing to the exceptional properties of the 2D layered *h*-BN, the impact of non-ideal factors on the device performance is minimized, such as interface traps at the heterojunction and SRH effect. In this work, GaN-based MIS blocks achieve a maximum V_{th} of 4.28 V and a maximum I_{on} of 2.12×10^{-2} A, showcasing competitive performance in comparison to existing reports. It is also possible to design an MIS block with an impressive *FOM* of 25.8 mW, by taking electric power tolerance into account, achieving a satisfactory equilibrium between V_{th} and I_{on}. We can design high power devices or high threshold voltage devices, through the rational use of structural and material properties, for the diversity of performance of the MIS block. This work provides a reference for the design and investigation of devices such as infrared detectors through incorporating novel 2D materials with traditional semiconductor heterogeneous and

mixed-dimensional integration, contributing to the advancement in both optics and microelectronics.

CRediT authorship contribution statement

Jiayi Qin: Writing – review & editing, Writing – original draft, Formal analysis, Data curation. **Ruiqi Jiang:** Writing – review & editing, Writing – original draft, Formal analysis, Data curation. **Man Luo:** Resources, Formal analysis. **Tiantian Cheng:** Formal analysis. **Yuxin Meng:** Data curation. **Yuanze Zu:** Formal analysis. **Jinzhong Zhang:** Writing – review & editing, Resources. **Johnny C. Ho:** Data curation. **Chenhui Yu:** Writing – review & editing, Funding acquisition. **Junhao Chu:** Writing – review & editing, Methodology.

Declaration of competing interest

The authors declare that they have no known competing financial interests or personal relationships that could have appeared to influence the work reported in this paper.

Data availability

Data will be made available on request.

Acknowledgements

The authors are grateful for financial support from the National Natural Science Foundation of China (Grant Nos. 62074085, 62104118 and 62074058)

References

[1] H. Cui, Z.Z. Qin, H.H. Sun, Z.G. Chen, W.P. Qin, Near-infrared light excitation of *h*-BN ultra-wide bandgap semiconductor, Appl. Phys. Lett. 121 (2022) 241101, https://doi.org/10.1063/5.0131613.

[2] L. Cigarini, M. Novotný, F. Karlický, Lattice dynamics in the conformational environment of multilayered hexagonal boron nitride (h-BN) results in peculiar infrared optical responses, PCCP 23 (2021) 7247–7260, https://doi.org/10.1039/d0cp06188c.

[3] M. Takamura, K. Watanabe, T. Taniguchi, Y. Taniyasu, Nanoscale infrared imaging and spectroscopy of few-layer hexagonal boron nitride, J. Appl. Phys. 132 (2022) 174301, https://doi.org/10.1063/5.0107821.

[4] Y.F. Chen, Y. Wang, Z. Wang, Y. Gu, Y. Ye, X.L. Chai, J.F. Ye, Y. Chen, R.Z. Xie, Y. Zhou, Z.G. Hu, Q. Li, L.L. Zhang, F. Wang, P. Wang, J.S. Miao, J.L. Wang, X. S. Chen, W. Lu, P. Zhou, W.D. Hu, Unipolar barrier photodetectors based on van der Waals heterostructures, Nat. Electron. 4 (2021) 357, https://doi.org/10.1038/s41928-021-00586-w.

[5] F. Wu, Q. Li, P. Wang, H. Xia, Z. Wang, Y. Wang, M. Luo, L. Chen, F.S. Chen, J. S. Miao, X.S. Chen, W. Lu, C.X. Shan, A.L. Pan, X. Wu, W.C. Ren, D. Jariwala, W. D. Hu, High efficiency and fast van der Waals hetero-photodiodes with a unilateral depletion region, Nat. Commun. 10 (2019) 4663, https://doi.org/10.1038/s41467-019-12707-3.

[6] W.D. Hu, Z.H. Ye, L. Liao, H.L. Chen, L. Chen, R.J. Ding, L. He, X.S. Chen, W. Lu, 128 x 128 long-wavelength/mid-wavelength two-color HgCdTe infrared focal plane array detector with ultralow spectral cross talk, Opt. Lett. 39 (2014) 5184–5187, https://doi.org/10.1364/OL.39.005184.

[7] Y. Hattori, T. Taniguchi, K. Watanabe, K. Nagashio, Determination of Carrier Polarity in Fowler-Nordheim Tunneling and Evidence of Fermi Level Pinning at the Hexagonal Boron Nitride/Metal Interface, ACS Appl Mater Interfaces 10 (2018) 11732–11738, https://doi.org/10.1021/acsami.7b18454.

[8] J.G. Wang, F.C. Ma, W.J. Liang, M.T. Sun, Electrical properties and applications of graphene, hexagonal boron nitride (*h*-BN), and graphene/*h*-BN heterostructures, Mater. Today Phys. 2 (2017) 6–34, https://doi.org/10.1016/j.mtphys.2017.07.001.

[9] S. Gupta, P. Joshi, R. Sachan, J. Narayan, Fabricating Graphene Oxide/*h*-BN Metal Insulator Semiconductor Diodes by Nanosecond Laser Irradiation, Nanomaterials (basel) 12 (2022), https://doi.org/10.3390/nano12152718.

[10] G.-H. Lee, Y.-J. Yu, C. Lee, C. Dean, K.L. Shepard, P. Kim, J. Hone, Electron tunneling through atomically flat and ultrathin hexagonal boron nitride, Appl. Phys. Lett. 99 (2011), https://doi.org/10.1063/1.3662043.

[11] F. Gao, H.Y. Chen, W. Feng, Y.X. Hu, H.M. Shang, B. Xu, J. Zhang, C.Y. Xu, P.A. Hu, High-performance van der Waals metal-insulator-semiconductor photodetector optimized with valence band matching, Adv. Funct. Mater. 31 (2021), https://doi.org/10.1002/adfm.202104359.

[12] P. Vuong, T. Moudakir, R. Gujrati, A. Srivastava, V. Ottapilakkal, S. Gautier, P. L. Voss, S. Sundaram, J.P. Salvestrini, A. Ougazzaden, Scaling up of Growth, Fabrication, and Device Transfer Process for GaN-based LEDs on *h*-BN Templates to 6-inch Sapphire Substrates, Adv. Mater. Technol. 8 (2023), https://doi.org/10.1002/admt.202300600.

[13] F. Liu, Y. Yu, Y.T. Zhang, X. Rong, T. Wang, X.T. Zheng, B.W. Sheng, L.Y. Yang, J. Q. Wei, X.P. Wang, X.B. Li, X.L. Yang, F.J. Xu, Z.X. Qin, Z.H. Zhang, B. Shen, X. Q. Wang, Hexagonal BN-assisted epitaxy of strain released GaN films for true green light-emitting diodes, Adv. Sci (weinh). 7 (2020) 2000917, https://doi.org/10.1002/advs.202000917.

[14] L. Ravi, M.A. Rather, K.L. Lin, C.T. Wu, T.Y. Yu, K.Y. Lai, J.I. Chyi, Epitaxial growth of GaN/AlN on h-BN/Si (111) by metal-organic chemical vapor deposition: An interface analysis, ACS Appl. Electron. Mater. 5 (2023) 146–154, https://doi.org/10.1021/acsaelm.2c01078.

[15] Y. Peng, Y.F. Yang, K. Xiao, Y.L. Yang, H.R. Ding, J.Y. Deng, W.H. Sun, Direct synthesis of vertical self-assembly oriented hexagonal boron nitride on Gallium Nitride and ultrahigh photoresponse ultraviolet photodetectors, Nanomaterials (basel) 13 (2023), https://doi.org/10.3390/nano13091546.

[16] S.K. Jain, M.X. Low, P.D. Taylor, S.A. Tawfik, M.J.S. Spencer, S. Kuriakose, A. Arash, C. Xu, S. Sriram, G. Gupta, M. Bhaskaran, S. Walia, 2D/3D Hybrid of MoS_2/GaN for a High-Performance Broadband Photodetector, ACS Appl. Electron. Mater. 3 (2021) 2407–2414, https://doi.org/10.1021/acsaelm.1c00299.

[17] P.S. Wu, L. Ye, L. Tong, P. Wang, Y. Wang, H.L. Wang, H.N. Ge, Z. Wang, Y. Gu, K. Zhang, Y.Y. Yu, M. Peng, F. Wang, M. Huang, P. Zhou, Van der Waals two-color infrared photodetector, Light: Sci. Appl. 11 (2022) 6, https://doi.org/10.1038/s41377-021-00694-4.

[18] Y.H. Lu, Z.Q. Wu, W.L. Xu, S.S. Lin, ZnO quantum dot-doped graphene/*h*-BN/GaN-heterostructure ultraviolet photodetector with extremely high responsivity, Nanotechnology 27 (2016) 48LT03, https://doi.org/10.1088/0957-4484/27/48/48LT03.

[19] D.A. Laleyan, S. Zhao, S.Y. Woo, H.N. Tran, H.B. Le, T. Szkopek, H. Guo, G. A. Botton, Z. Mi, AlN/*h*-BN Heterostructures for Mg Dopant-Free Deep Ultraviolet Photonics, Nano Lett 17 (2017) 3738–3743, https://doi.org/10.1021/acs.nanolett.7b01068.

[20] M. Whiteside, S. Arulkumaran, G.I. Ng, Demonstration of vertically-ordered *h*-BN/AlGaN/GaN metal-insulator-semiconductor high-electron-mobility transistors on Si substrate, Mater. Sci. Eng. B 270 (2021), https://doi.org/10.1016/j.mseb.2021.115224.

[21] S. Singh, T. Chaudhary, G. Khanna, Recent Advancements in Wide Band Semiconductors (SiC and GaN) Technology for Future Devices, SILICON 14 (2021) 5793–5800, https://doi.org/10.1007/s12633-021-01362-3.

[22] T. Pu, U. Younis, H.C. Chiu, K. Xu, H.C. Kuo, X. Liu, Review of Recent Progress on Vertical GaN-Based PN Diodes, Nanoscale Res Lett 16 (2021) 101, https://doi.org/10.1186/s11671-021-03554-7.

[23] J. Wang, Q. Yao, C.W. Huang, X. Zou, L. Liao, S. Chen, Z. Fan, K. Zhang, W. Wu, X. Xiao, C. Jiang, W.W. Wu, High Mobility MoS_2 Transistor with Low Schottky Barrier Contact by Using Atomic Thick *h*-BN as a Tunneling Layer, Adv Mater 28 (2016) 8302–8308, https://doi.org/10.1002/adma.201602757.

[24] Y.R. Kim, T.L. Phan, Y.S. Shin, W.T. Kang, U.Y. Won, I. Lee, J.E. Kim, K. Kim, Y. H. Lee, W.J. Yu, Unveiling the Hot Carrier Distribution in Vertical Graphene/*h*-BN/Au van der Waals Heterostructures for High-Performance Photodetector, ACS Appl Mater Interfaces 12 (2020) 10772–10780, https://doi.org/10.1021/acsami.9b19904.

[25] H. Du, Z. Xu, Z. Wei, D. Li, S. Chen, W. Tian, P. Zhang, Y.-Y. Lyu, H. Sun, Y.-L. Wang, H. Wang, P. Wu, High-energy electron local injection in top-gated metallic superconductor switch, Supercond. Sci. Technol. 36 (2023), https://doi.org/10.1088/1361-6668/ace65f.

[26] J. Szmytkowski, Quenching of bright and dark excitons via deep states in the presence of SRH recombination in 2D monolayer materials, J Phys Condens Matter 51 (2022), https://doi.org/10.1088/1361-648X/ac9d7e.

[27] G. Sabui, P.J. Parbrook, M. Arredondo-Arechavala, Z.J. Shen, Modeling and simulation of bulk gallium nitride power semiconductor devices, AIP Adv. 6 (2016), https://doi.org/10.1063/1.4948794.

[28] A. Maity, S.J. Grenadier, J. Li, J.Y. Lin, H.X. Jiang, Hexagonal boron nitride: Epitaxial growth and device applications, Prog. Quantum Electron. 76 (2021), https://doi.org/10.1016/j.pquantelec.2020.100302.

[29] Y. Ji, B. Calderon, Y. Han, P. Cueva, N.R. Jungwirth, H.A. Alsalman, J. Hwang, G. D. Fuchs, D.A. Muller, M.G. Spencer, Chemical Vapor Deposition Growth of Large Single-Crystal Mono-, Bi-, Tri-Layer Hexagonal Boron Nitride and Their Interlayer Stacking, ACS Nano 11 (2017) 12057–12066, https://doi.org/10.1021/acsnano.7b04841.

[30] J.Y. Qin, M. Luo, T.T. Cheng, Y.X. Meng, Y.Z. Zu, X. Wang, C.H. Yu, Extracting the effective mass of fewer layers 2D *h*-BN nanosheets using the Fowler Nordheim tunneling model. J. Infrared Millimeter Waves, in press.

[31] Y. Cai, Y. Liu, Y. Xie, Y. Zou, C. Gao, Y. Zhao, S. Liu, H.X. Xu, J. Shi, S.S. Guo, C. L. Sun, Band structure, effective mass, and carrier mobility of few-layer *h*-AlN under layer and strain engineering, APL Mater. 8 (2020), https://doi.org/10.1063/1.5139664.

[32] J. Li, J. Wang, X. Zhang, C. Elias, G. Ye, D. Evans, G. Eda, J.M. Redwing, G. Cassabois, B. Gil, P. Valvin, R. He, B. Liu, J.H. Edgar, Hexagonal Boron Nitride Crystal Growth from Iron, a Single Component Flux, ACS Nano 15 (2021) 7032–7039, https://doi.org/10.1021/acsnano.1c00115.

[33] S. Naghdi, G. Sanchez-Arriaga, K.Y. Rhee, Tuning the work function of graphene toward application as anode and cathode, J. Alloy. Compd. 805 (2019) 1117–1134, https://doi.org/10.1016/j.jallcom.2019.07.187.

[34] Z.M. Gibbs, F. Ricci, G. Li, H. Zhu, K. Persson, G. Ceder, G. Hautier, A. Jain, G. J. Snyder, Effective mass and Fermi surface complexity factor from ab initio band

structure calculations, NPJ Comput. Mater. 3 (2017), https://doi.org/10.1038/s41524-017-0013-3.
[35] Y.-S. Kim, M. Marsman, G. Kresse, F. Tran, P. Blaha, Towards efficient band structure and effective mass calculations for III-V direct band-gap semiconductors, Phys. Rev. B 82 (2010) 205212, https://doi.org/10.1103/PhysRevB.82.205212.
[36] A.N. Tallarico, S. Stoffels, N. Posthuma, B. Bakeroot, S. Decoutere, E. Sangiorgi, C. Fiegna, Gate Reliability of p-GaN HEMT With Gate Metal Retraction, IEEE Trans. Electron Devices 66 (2019) 4829–4835, https://doi.org/10.1109/ted.2019.2938598.
[37] Y. Zhang, M. Sun, D. Piedra, M. Azize, X. Zhang, T. Fujishima, T. Palacios, GaN-on-Si Vertical Schottky and p-n Diodes, IEEE Electron Device Lett. 35 (2014) 618–620, https://doi.org/10.1109/LED.2014.2314637.
[38] R.Z. Xie, Q. Li, P. Wang, X.S. Chen, W. Lu, H.J. Guo, L. Chen, W.D. Hu, Spatial description theory of narrow-band single-carrier avalanche photodetectors, Opt. Express 29 (2021) 16432–16446, https://doi.org/10.1364/OE.418110.
[39] W.-H. Lin, V.W. Brar, D. Jariwala, M.C. Sherrott, W.-S. Tseng, C.-I. Wu, N.-C. Yeh, H.A. Atwater, Atomic-Scale Structural and Chemical Characterization of Hexagonal Boron Nitride Layers Synthesized at the Wafer-Scale with Monolayer Thickness Control, Chem. Mater. 29 (2017) 4700–4707, https://doi.org/10.1021/acs.chemmater.7b00183.
[40] S.K. Jang, J. Youn, Y.J. Song, S. Lee, Synthesis and Characterization of Hexagonal Boron Nitride as a Gate Dielectric, Sci Rep 6 (2016) 30449, https://doi.org/10.1038/srep30449.
[41] Z. Xu, H. Tian, A. Khanaki, R. Zheng, M. Suja, J. Liu, Large-area growth of multi-layer hexagonal boron nitride on polished cobalt foils by plasma-assisted molecular beam epitaxy, Sci Rep 7 (2017) 43100, https://doi.org/10.1038/srep43100.
[42] F. Palumbo, X. Liang, B. Yuan, Y. Shi, F. Hui, M.A. Villena, M. Lanza, Bimodal Dielectric Breakdown in Electronic Devices Using Chemical Vapor Deposited Hexagonal Boron Nitride as Dielectric, Adv. Electron. Mater. 4 (2018), https://doi.org/10.1002/aelm.201700506.
[43] K. Zhang, F.L. Yap, K. Li, C.T. Ng, L.J. Li, K.P. Loh, Large Scale Graphene/Hexagonal Boron Nitride Heterostructure for Tunable Plasmonics, Adv. Funct. Mater. 24 (2013) 731–738, https://doi.org/10.1002/adfm.201302009.
[44] L. Wu, H.X. Liu, J.F. Lin, S.L. Wang, Volatile and nonvolatile memory operations implemented in a Pt/HfO_2/Ti memristor, IEEE Trans. Electron Devices 68 (2021) 1622–1626, https://doi.org/10.1109/ted.2021.3061033.
[45] T. Zhang, Y. Wang, Y.N. Zhang, Y.G. Lv, J. Ning, Y.C. Zhang, H. Zhou, X.L. Duan, J. C. Zhang, Y. Hao, Comprehensive annealing effects on AlGaN/GaN Schottky barrier diodes With different work-function metals, IEEE Trans. Electron Devices 68 (2021) 2661–2666, https://doi.org/10.1109/ted.2021.3074896.
[46] F. Wang, Z.Y. Liu, T. Zhang, M.S. Long, X.X. Wang, R.Z. Xie, H.N. Ge, H. Wang, J. Hou, Y. Gu, X. Hu, Z. Song, S.F. Wang, Q.S. Dong, K.C. Liao, Y.B. Tu, T. Han, F. Li, Z.Y. Zhang, X.Y. Hou, S.L. Wang, L. Li, X.A. Zhang, D.X. Zhao, C.X. Shan, L. Shan, W.D. Hu, Fully depleted self-aligned heterosandwiched Van der waals photodetectors, Adv. Mater. 34 (2022) 2203283, https://doi.org/10.1002/adma.202203283.
[47] A. Rawat, M. Meer, V.K. Surana, N. Bhardwaj, V. Pendem, N.S. Garigapati, Y. Yadav, S. Ganguly, D. Saha, Thermally Grown TiO_2 and Al_2O_3 for GaN-Based MOS-HEMTs, IEEE Trans. Electron Devices 65 (2018) 3725–3731, https://doi.org/10.1109/ted.2018.2857468.
[48] Y. Cai, Y. Wang, Y. Liang, Y. Zhang, W. Liu, H. Wen, I.Z. Mitrovic, C. Zhao, Effect of High-k Passivation Layer on High Voltage Properties of GaN Metal-Insulator-Semiconductor Devices, IEEE Access 8 (2020) 95642–95649, https://doi.org/10.1109/access.2020.2995906.
[49] K. Onishi, T. Kobayashi, H. Mizobata, M. Nozaki, A. Yoshigoe, T. Shimura, H. Watanabe, Formation of high-quality SiO_2/GaN interfaces with suppressed Ga-oxide interlayer via sputter deposition of SiO_2, Jpn. J. Appl. Phys. 62 (2023). https://doi.org/10.35848/1347-4065/acd1ca.
[50] Y.-S. Lin, C.-C. Lu, Improved AlGaN/GaN Metal-Oxide-Semiconductor High-Electron Mobility Transistors With TiO_2 Gate Dielectric Annealed in Nitrogen, IEEE Trans. Electron Devices 65 (2018) 783–787, https://doi.org/10.1109/ted.2017.2781141.
[51] H. Chandrasekar, S. Kumar, K.L. Ganapathi, S. Prabhu, S.B. Dolmanan, S. Tripathy, S. Raghavan, K.N. Bhat, S. Mohan, R. Muralidharan, N. Bhat, D.N. Nath, Dielectric Engineering of HfO_2 Gate-Stacks for Normally-ON GaN HEMTs on 200-mm Silicon Substrates, IEEE Trans. Electron Devices 65 (2018) 3711–3718, https://doi.org/10.1109/ted.2018.2856773.
[52] H. Jiang, C. Liu, K.W. Ng, C.W. Tang, K.M. Lau, High-Performance AlGaN/GaN/Si Power MOSHEMTs With ZrO_2 Gate Dielectric, IEEE Trans. Electron Devices 65 (2018) 5337–5342, https://doi.org/10.1109/ted.2018.2874075.
[53] J.J. Zhu, X.H. Ma, Y. Xie, B. Hou, W.W. Chen, J.C. Zhang, Y. Hao, Improved interface and transport properties of AlGaN/GaN MIS-HEMTs with PEALD-Grown AlN gate dielectric, IEEE Trans. Electron Devices 62 (2015) 512–518, https://doi.org/10.1109/ted.2014.2377781.
[54] V.N. Reddy, R. Padma, K.R. Gunasekhar, Analysis of electronic parameters and frequency-dependent properties of Au/NiO/n-GaN heterojunctions, Appl. Phys. A 124 (2018), https://doi.org/10.1007/s00339-017-1483-3.
[55] B. Ren, M. Liao, M. Sumiya, J. Li, L. Wang, X. Liu, Y. Koide, L. Sang, Layered boron nitride enabling high-performance AlGaN/GaN high electron mobility transistor, J. Alloy. Compd. 829 (2020), https://doi.org/10.1016/j.jallcom.2020.154542.
[56] W.D. Hu, X.S. Chen, Z.H. Ye, J. Zhang, F. Yin, C. Lin, Z.F. Li, W Lu, Accurate simulation of temperature-dependent dark current in HgCdTe infrared detectors assisted by analytical modeling, J. Electron. Mater. 39 (2010) 981–995, https://doi.org/10.1007/s11664-010-1121-8.
[57] W.D. Hu, X.S. Chen, Z.H. Ye, W. Lu, A hybrid surface passivation on HgCdTe long wave infrared detector with in-situ CdTe deposition and high-density hydrogen plasma modification, Appl. Phys. Lett. 99 (2011) 091101, https://doi.org/10.1063/1.3633103.
[58] C.E. Dreyer, A. Alkauskas, J.L. Lyons, J.S. Speck, C.G. Van de Walle, Gallium vacancy complexes as a cause of Shockley-Read-Hall recombination in III-nitride light emitters, Appl. Phys. Lett. 108 (2016), https://doi.org/10.1063/1.4942674.
[59] F. Nasim, A.S. Bhatti, Influence of different metal over-layers on the electrical behaviour of the MIS Schottky diodes, Int. J. Electron. 100 (2013) 1228–1239, https://doi.org/10.1080/00207217.2012.743077.
[60] T. Xu, Z. Tang, Z. Zhou, B. Zhou, Simulation Optimization of AlGaN/GaN SBD with Field Plate Structures and Recessed Anode, Micromachines (basel) 14 (2023), https://doi.org/10.3390/mi14061121.
[61] S. Han, T. Kwak, U. Choi, H. Kang, G. Yoo, S.-w. Kim, O. Nam, Electrical Characteristics of Metal–Insulator Diamond Semiconductor Schottky Barrier Diode Grown on Heteroepitaxial Diamond Substrate, Phys. Status Solidi (A), 220 (2023). https://doi.org/10.1002/pssa.202200680.
[62] N.N.K. Reddy, C. Kukkambakam, V. Manjunath, V.R.M. Reddy, Analysis of Double Gaussian Distribution at the Interface of Ni/Ta2O5/P-Si Schottky Barrier Diodes Using Temperature Dependent Current-Voltage (I-V) Measurements, SILICON 13 (2020) 65–71, https://doi.org/10.1007/s12633-020-00407-3.
[63] N.K.R. Nallabala, V.K. Kummara, Y. Chinnappa, P.P. George, V. Manjunath, J. Sanniboina, S.M. Reddy, N.R. Gangasani, A Study on Annealing Process Influenced Electrical Properties of Ni/CeO_2/p-Si/Al Schottky Barrier Diodes, Macromol. Symp. 398 (2021), https://doi.org/10.1002/masy.202000228.
[64] H. Jeong, H.M. Oh, S. Bang, H.J. Jeong, S.J. An, G.H. Han, H. Kim, S.J. Yun, K. K. Kim, J.C. Park, Y.H. Lee, G. Lerondel, M.S. Jeong, Metal-Insulator-Semiconductor Diode Consisting of Two-Dimensional Nanomaterials, Nano Lett 16 (2016) 1858–1862, https://doi.org/10.1021/acs.nanolett.5b04936.
[65] Z.L. Li, K. Yuan, Y. Ye, High rectification ratio metal-insulator-semiconductor tunnel diode based on single-layer MoS_2, Nanotechnology 31 (2020) 075202, https://doi.org/10.1088/1361-6528/ab53b7.
[66] K. Sasikumar, R. Bharathikannan, M. Raja, B. Mohanbabu, Fabrication and characterization of rare earth (Ce, Gd, and Y) doped ZrO2 based metal-insulator-semiconductor (MIS) type Schottky barrier diodes, Superlattices Microstruct. 139 (2020), https://doi.org/10.1016/j.spmi.2020.106424.
[67] C. Yang, H. Fu, P.-Y. Su, H. Liu, K. Fu, X. Huang, T.-H. Yang, H. Chen, J. Zhou, X. Deng, J. Montes, X. Qi, F.A. Ponce, Y. Zhao, Demonstration of GaN-based metal–insulator–semiconductor junction by hydrogen plasma treatment, Appl. Phys. Lett. 117 (2020), https://doi.org/10.1063/5.0018473.
[68] T. Zhang, Y.N. Zhang, J.C. Zhang, X.D. Li, Y.G. Lv, Y. Hao, Current transport mechanism of high-performance novel GaN MIS diode, IEEE Electron Device Lett. 42 (2021) 304–307, https://doi.org/10.1109/led.2021.3051690.